● *Original Contribution*

EFFECTS OF DROPLET COMPOSITION ON NANODROPLET-MEDIATED HISTOTRIPSY

ELI VLAISAVLJEVICH,* OMER AYDIN,* YASEMIN YUKSEL DURMAZ,*[†] KUANG-WEI LIN,*
BRIAN FOWLKES,*[‡] ZHEN XU,*[§] and MOHAMED E. H. ELSAYED*[¶]

*Department of Biomedical Engineering, University of Michigan, Ann Arbor, MI, USA; [†]Department of Biomedical
Engineering, Schools of Engineering and Natural Science, Istanbul Medipol University, Istanbul, Turkey; [‡]Department of
Radiology, University of Michigan, Ann Arbor, MI, USA; [§]Division of Pediatric Cardiology, Department of Pediatrics and
Communicable Diseases, University of Michigan, Ann Arbor, MI, USA; and [¶]Macromolecular Science and Engineering
Program, University of Michigan, Ann Arbor, MI, USA

Abstract—Nanodroplet-mediated histotripsy (NMH) is a targeted ablation technique combining histotripsy with nanodroplets that can be selectively delivered to tumor cells. In two previous studies, polymer-encapsulated perfluoropentane nanodroplets were used to generate well-defined ablation similar to that obtained with histotripsy, but at significantly lower pressure, when NMH therapy was applied at a pulse repetition frequency (PRF) of 10 Hz. However, cavitation was not maintained over multiple pulses when ultrasound was applied at a lower PRF (*i.e.*, 1–5 Hz). We hypothesized that nanodroplets with a higher-boiling-point perfluorocarbon core would provide sustainable cavitation nuclei, allowing cavitation to be maintained over multiple pulses, even at low PRF, which is needed for efficient and complete tissue fractionation *via* histotripsy. To test this hypothesis, we investigated the effects of droplet composition on NMH therapy by applying histotripsy at various frequencies (345 kHz, 500 kHz, 1.5 MHz, 3 MHz) to tissue phantoms containing perfluoropentane (PFP, boiling point ~29°C, surface tension ~9.5 mN/m) and perfluorohexane (PFH, boiling point ~56°C, surface tension ~11.9 mN/m) nanodroplets. First, the effects of droplet composition on the NMH cavitation threshold were investigated, with results revealing a significant decrease (>10 MPa) in the peak negative pressure ($p-$) cavitation threshold for both types of nanodroplets compared with controls. A slight decrease (~1–3 MPa) in threshold was observed for PFP phantoms compared with PFH phantoms. Next, the ability of nanodroplets to function as sustainable cavitation nuclei over multiple pulses was investigated, with results revealing that PFH nanodroplets were sustainable cavitation nuclei over 1,000 pulses, whereas PFP nanodroplets were destroyed during the first few pulses (<50 pulses), likely because of the lower boiling point. Finally, tissue phantoms containing a layer of embedded red blood cells were used to compare the damage generated for NMH treatments using PFP and PFH droplets, with results indicating that PFH nanodroplets significantly improved NMH ablation, allowing for well-defined lesions to be generated at all frequencies and PRFs tested. Overall, the results of this study provide significant insight into the role of droplet composition in NMH therapy and provide a rational basis to tailor droplet parameters to improve NMH tissue fractionation. (E-mail: melsayed@umich.edu or http://www.bme.umich.edu/centlab.php)   © 2016 World Federation for Ultrasound in Medicine & Biology.

Key Words: Nanodroplet, Histotripsy, Perfluoropentane, Perfluorohexane, Cavitation.

INTRODUCTION

Histotripsy is a non-invasive tissue ablation method that controllably fractionates soft tissue through cavitation generated by high-pressure, short-duration ultrasound pulses (Parsons et al. 2006a; Roberts et al. 2006; Xu et al. 2005b). Histotripsy depends on the initiation and maintenance of a dense cavitation bubble cloud to produce mechanical tissue fractionation (Parsons et al. 2007; Xu et al. 2005a). Previous work has indicated that by use of a 1-2 cycle pulse with a single dominant

negative pressure phase, cavitation bubbles can be reproducibly generated in tissue when the peak negative pressure ($p-$) is raised above the histotripsy intrinsic threshold of ~25–30 MPa (Maxwell et al. 2013; Vlaisavljevich et al. 2015b). To effectively fractionate tissue into acellular debris, histotripsy requires a dense cavitation bubble cloud to be initiated and maintained over multiple pulses (often >100) until the tissue is completely fractionated into a liquid-appearing homogenate with no cellular structures remaining (Hall et al. 2007; Roberts et al. 2006; Xu et al. 2005b). Histotripsy is currently being studied for many clinical applications in which non-invasive tissue removal is desired, including benign prostatic hyperplasia (Hempel et al. 2011), deep vein thrombosis (Maxwell et al. 2011), congenital heart disease (Owens et al. 2011; Xu et al. 2010) and cancer (Styn et al. 2010; Vlaisavljevich et al. 2013b).

Although histotripsy has shown promise for many clinical applications including tumor ablation, this approach is limited to applications in which the target tissue can be identified and imaged before treatment, which is often not feasible in cancer patients with many small tumor nodules and micrometastases. As a result, our group has developed a targeted ablation approach combining polymer-encapsulated nanodroplets with histotripsy (Vlaisavljevich et al. 2013a, 2015a; Yuksel Durmaz et al. 2014). This nanodroplet-mediated histotripsy (NMH) approach takes advantage of the significantly reduced cavitation threshold of the nanodroplets, allowing cavitation to be selectively generated only in regions where nanodroplets localize (Vlaisavljevich et al. 2013a). NMH has the potential for selective ablation of tumors given the small size (~100–400 nm) of the synthesized nanodroplets, which enables their diffusion across the leaky tumor vasculature and preferential accumulation in the tumor tissue (Vlaisavljevich et al. 2013a; Yuksel Durmaz et al. 2014). Previous work has indicated that NMH can be used to create well-defined ablation similar to that obtained with histotripsy, but at significantly lower pressure, and has also indicated the potential to use NMH for simultaneous multifocal ablation (Vlaisavljevich et al. 2013a). Furthermore, a previous study by Yuksel Durmaz et al. (2014) investigated the optimal characteristics of polymer-encapsulated perfluoropentane (PFP) nanodroplets, with results showing optimal NMH ablation for nanodroplets with a shell-crosslinked triblock amphiphilic co-polymer composed of a poly(ethylene glycol) block that forms a biocompatible corona, a poly(acrylic acid) middle block reacting with the crosslinker to form a flexible shell and a poly(heptadecafluorodecyl methacrylate-co-methyl methacrylate) fluorinated hydrophobic block encapsulating 2% (v/v) PFP. However, although this previous study determined the optimal conditions for PFP

nanodroplets, the effects of perfluorocarbon boiling temperature on NMH therapy have not been previously investigated.

In this study, we compare PFP (boiling point ~29°C) and perfluorohexane (PFH, boiling point ~56°C) nanodroplets for NMH therapy. On the basis of previous work comparing PFP and PFH droplets for acoustic droplet vaporization (Fabiilli et al. 2009; Giesecke and Hynynen 2003), we hypothesize that PFH nanodroplets will have a slightly higher cavitation threshold than PFP droplets, but the cavitation threshold of both droplets will be significantly lower than the histotripsy intrinsic threshold. To test this hypothesis, tissue phantoms containing PFP nanodroplets, PFH nanodroplets, and no nanodroplets were exposed to histotripsy pulses produced by 345-kHz, 500-kHz, 1.5-MHz, and 3-MHz custom-built histotripsy transducers. The probability of generating inertial cavitation from a single 1-2 cycle histotripsy pulse was measured, with the cavitation threshold defined as the peak negative pressure at which the probability of generating cavitation, p_{cav}, from a single histotripsy pulse was 0.5. In addition to the effects of droplet composition on the cavitation threshold, we also investigated the effects of droplet composition on cavitation sustainability over multiple histotripsy pulses. In previous studies, PFP nanodroplets were used to create consistent, well-defined fractionation at pressure levels (11–20 MPa) significantly below the histotripsy intrinsic threshold (~26–30 MPa) in tissue phantoms at a pulse repetition frequency (PRF) of 10 Hz by maintaining cavitation over multiple pulses (Vlaisavljevich et al. 2013a; Yuksel Durmaz et al. 2014). However, it was also observed that cavitation was not maintained over multiple pulses when ultrasound was applied at a lower PRF (1 Hz) (Vlaisavljevich et al. 2013a, 2015a; Yuksel Durmaz et al. 2014). A low PRF (1 Hz) has been found to produce more efficient tissue fractionation and is not affected by the cavitation memory effect, in which residual gas bubbles from previous cavitation events function as nuclei for generating cavitation on a subsequent pulse (Wang et al. 2012). This result suggests that PFP nanodroplets are destroyed during the first few pulses, requiring cavitation on subsequent pulses to be generated from residual nuclei remaining from previous pulses. We hypothesize that because of their higher boiling point, PFH nanodroplets will re-condense into a liquid after cavitation and remain as sustainable nuclei over multiple (>100) pulses, allowing cavitation to be maintained over multiple pulses even at low PRF. To test this hypothesis, 1,000 histotripsy pulses were applied to a single focal zone tissue in phantoms containing PFP and PFH nanodroplets, and the numbers of NMH bubbles generated were compared after each pulse. In addition,

tissue phantoms containing a layer of embedded red blood cells were used to compare the damage generated for NMH treatments using PFP and PFH droplets. Overall, these results will improve our understanding of the NMH process and help to determine the optimal nanodroplet characteristics for NMH therapy.

METHODS

Materials

Methyl methacrylate (MMA, 99%, Sigma-Aldrich, St. Louis, MO, USA), 3,3,4,4,5,5,6,6,7,7,8,8,9,9, 10,10,10-heptadecafluorodecyl methacrylate (HDFMA, 97%, Sigma-Aldrich), *tert*-butyl acrylate (tBA, 98%, Sigma-Aldrich), and *N, N, N′, N″, N‴*-pentamethyldiethylenetriamine (PMDETA, 99%, Sigma-Aldrich) were passed through a basic alumina column to remove the inhibitor. Copper(I) bromide (CuBr, 99.9%, Sigma-Aldrich), 2-bromoisobutyryl bromide (Fluka, >97%, Buchs, Switzerland), tetrahydrofuran anhydrous (THF, >99.9%, Sigma-Aldrich), *N,N′*-dicyclohexylcarbodiimide (DCC, 99%, Sigma-Aldrich), dimethylaminopyridine (DMAP, 99%, Acros, Geel, Belgium), 4-pentynoic acid (Sigma-Aldrich, 99%), furan (Sigma-Aldrich, ≥99%), maleic anhydride (Fluka, ≥99%), 9-anthracene methanol (Aldrich, ≥99%), PFP (97% ca. 85% *n*-isomer, Alfa Aesar, Ward Hill, MA), PFH (>98%, SynQuest Lab, Alachua, FL), *N*-hydroxysuccinimide (NHS, 97%, Fluka), *N*-(3-dimethylaminopropyl)-*N*-ethylcarbodiimide hydrochloride (EDC, >98%, Fluka), poly(ethylene glycol) monomethylether (Me-PEG, M_n = 2,000 g/mol, Sigma-Aldrich), sodium azide (NaN$_3$, 99%, Acros), 2-(*N*-morpholino)ethanesulfonic acid monohydrate (MES, 99%, Acros), triethylamine (TEA, ≥99%, Sigma-Aldrich), trifluoroacetic acid (TFA, 99%, Acros), ethylene carbonate (98%, Sigma-Aldrich), 2,2′-(ethylenedioxy)-bis(ethylamine) (98%, Sigma-Aldrich) agarose powder (type VII, Sigma-Aldrich), citrate phosphate–dextrose (CPD, Sigma-Aldrich), heptane fraction (>99%, Sigma-Aldrich) and dicholoromethane (DCM or CH$_2$Cl$_2$, >99.5%, Sigma-Aldrich) were used as received.

Nanodroplet formulation and characterization

A well-defined, triblock amphiphilic co-polymer containing a hydrophilic PEG block, a middle block poly(acrylic acid) (PAA) block and a hydrophobic random co-polymer of HDFMA and MMA was synthesized using a combination of atom transfer radical polymerization (ATRP) and "click" coupling techniques (Fig. 1), as previously described (Yuksel Durmaz et al. 2014). The synthesized P(HDFMA$_8$-*co*-MMA$_{20}$)-*b*-PAA$_{12}$-*b*-PEG$_{45}$ triblock amphiphilic copolymer was used to prepare PFP- and PFH-loaded nanodroplets. Briefly, the co-polymers were dissolved in tetrahydrofuran (THF, 0.2%

w/v) and cooled to 0°C before the addition of PFP (2% v/v) or PFH (2% v/v) while vigorously stirring the co-polymer–perfluorocarbon mixture. An equal amount of de-ionized water was added dropwise to this solution mixture to initiate micelle formation, and the mixture was stirred for 1 h in an ice bath. The micelle solution was transferred into a dialysis bag (MWCO of 1 kDa, Spectrum, Rancho Dominguez, CA, USA) and dialyzed overnight against ice-cold MES solution (pH 5.5) to remove the THF and obtain a milky solution of non-crosslinked PFP-loaded nanodroplets and non-crosslinked PFH-loaded nanodroplets. The milky nanodroplet solutions were transferred to round-bottom flasks and mixed with the 2,2′-(ethylenedioxy)-bis(ethylamine) crosslinker, which reacts with the carboxyl groups of the central PAA block in the co-polymer *via* NHS/EDC coupling chemistry, forming crosslinked nanodroplets with a flexible polymer shell. Shell-crosslinked nanodroplets were dialyzed against ice-cold water for 12 h to remove unreacted crosslinker and reaction by-products.

Concentration and size distribution of the nanodroplets were measured using nanoparticle tracking analysis (NTA). Briefly, the NanoSight LM10 (Malvern Instruments, Amesbury, UK), equipped with a temperature-controlled 405-nm laser module, high-sensitivity scientific complementary metal–oxide–semiconductor (sCMOS) camera (Hamamatsu, Orca, Hamamatsu City, Japan) and a syringe pump was used for collection of NTA data. On dilution of the nanodroplet solution to the appropriate particle concentration with de-ionized water, image capture and analysis were carried out using the NTA software (Version 3.0, Build 0066) at 37°C. Concentration and size distribution of the nanodroplets in each sample were analyzed using five videos per sample, each lasting 60 s. Based on these videos, nanodroplet concentration was plotted as a function of droplet size, with the error bars representing the standard deviation of the repeat measurements of each sample. The mean size and standard deviations obtained with the NTA software correspond to arithmetical values calculated with the sizes of all particles analyzed for each sample (n = 5).

Preparation of tissue phantoms

Agarose phantoms were used to provide a well-controlled viscoelastic medium for this study. Tissue phantoms containing 1% (w/w) agarose were prepared by slowly mixing agarose powder (agarose type VII, Sigma-Aldrich) into saline solution (0.9% sodium chloride, Hospira, Lake Forest, IL, USA) heated to boiling temperature. The solution was stirred on a hot plate until the gel turned completely transparent and then allowed to boil for 10 min. After boiling, solutions were allowed to cool and were degassed under a partial vacuum (~20 kPa, absolute) for 30 min. After degassing, phantoms
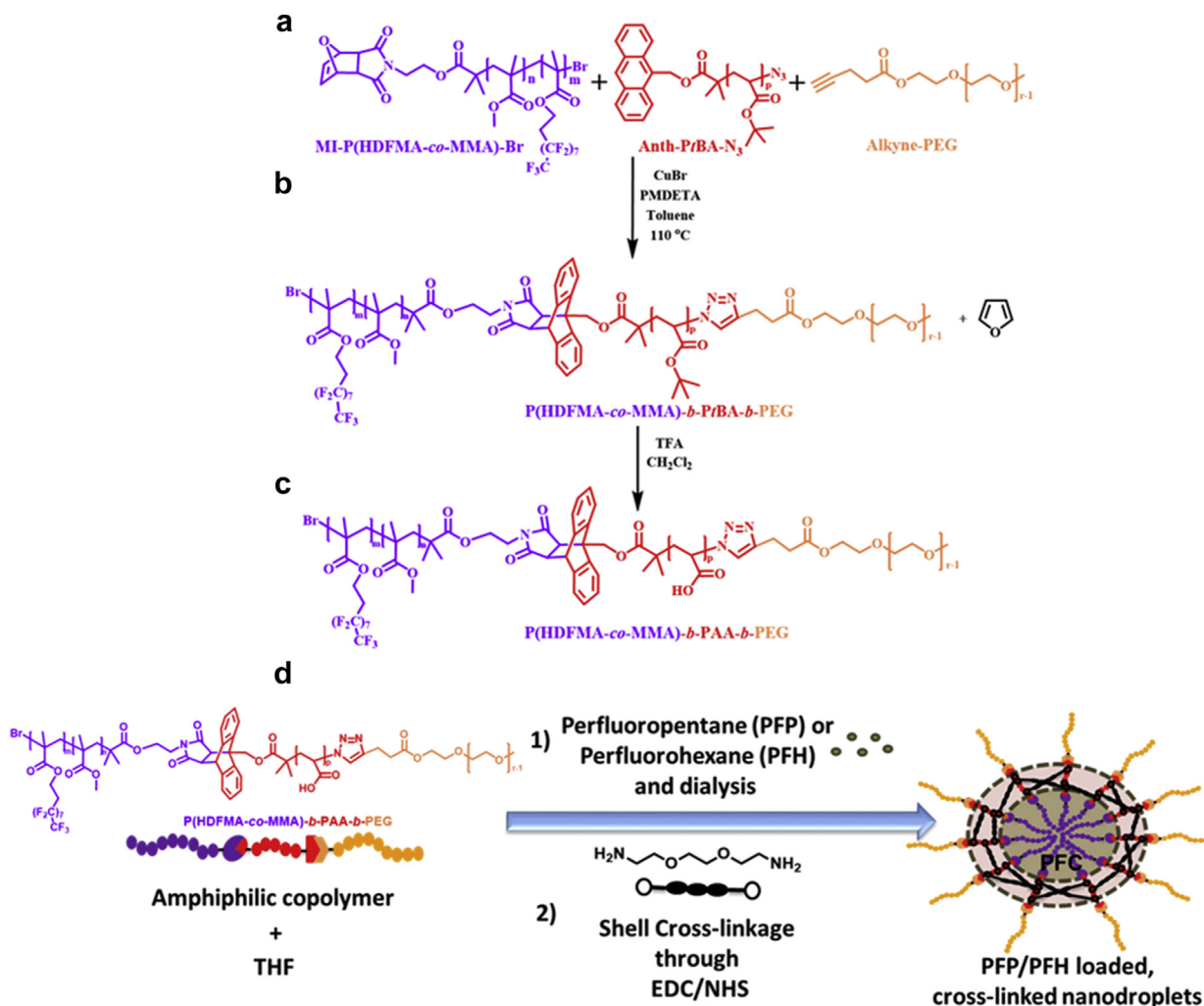
Fig. 1. Synthesis of the P(HDFMA-*co*-MMA)-*b*-P*t*BA-*b*-PEG triblock co-polymer and formulation of PFP- and PFH-loaded nanodroplets (a) The chemical structure of each block and (b) the one-pot "click" reaction to obtain P(HDFMA-*co*-MMA)-*b*-P*t*BA-*b*-PEG co-polymer. (c) Hydrolysis of the *t*BA group to obtain the P(HDFMA-*co*-MMA)-*b*-PAA-*b*-PEG co-polymer. (d) Formulation of the P(HDFMA-*co*-MMA)-*b*-P*t*BA-*b*-PEG co-polymer into PFP- and PFH-loaded nanodroplets. PFH = perfluorohexane, PFP = perfluoropentane, HDFMA = 3,3,4, 4,5,5,6,6,7,7,8,8,9,9,10,10,10-heptadecafluorodecyl methacrylate, *t*BA = *tert*-butyl acrylate, MMA = methyl methacrylate, PEG = poly(ethylene glycol), PMDETA = *N*, *N*, *N′*, *N″*, *N″*-pentamethyldiethylenetriamine, EDC = *N*-(3-dimethylaminopropyl)-*N*-ethylcarbodiimide hydrochloride, TFA = trifluoroacetic acid, NHS = *N*-hydroxysuccinimide, THF = tetrahydrofuran.

containing nanodroplets were prepared by slowly adding the nanodroplets (2.0×10^8 particles/mL) into the agarose solution while stirring. The agarose mixtures were poured into rectangular polycarbonate holders with acoustic windows and placed in a refrigerator at 4°C to allow the solution to solidify, forming tissue phantoms with embedded PFP or PFH nanodroplets or without nanodroplets (control). The temperature of the agarose was ~40°C when the nanodroplets were added. As this temperature is close to the temperature at which the NTA analysis was performed (37°C), it was expected that the size and concentration of nanodroplets would not be significantly affected by the casting process. This

hypothesis is further supported by previous studies indicating that PFP and PFH nanodroplets have vaporization temperatures much higher than their reported boiling points. For example, the vaporization temperatures of PFP and PFH nanodroplets size between 250 and 350 nm have been reported to be higher than 80°C and 140°C, respectively, suggesting that the droplets will remain stable during the casting process (40°C) and experimental temperatures (37°C) (Rapoport et al. 2009; Sheeran et al. 2011).

For cell fractionation experiments, tissue phantoms with a red blood cell (RBC) layer were prepared using porcine RBCs in 0.9% isotonic saline and 1% agarose

solutions with PFP or PFH nanodroplets. Fresh porcine blood was obtained from research patients in an unrelated study and added to an anticoagulant solution of CPD with a CPD-to-blood ratio of 1:9 mL. Whole blood was separated in a centrifuge at 3,000 rpm for 10 min. The plasma and white buffy coat were removed, and the RBCs were saved for addition to the phantom. To prepare the RBC phantom, an initial layer of 1% agarose mixture (with PFP or PFH nanodroplets) was poured into a rectangular polycarbonate housing to fill half of it at 40°C. The housing was placed in a refrigerator at 4°C to allow the agarose to cool and solidify. The remaining solution was kept at 40°C. A small amount of agarose solution was mixed with the RBCs (5% v/v). The frame with solidified agarose was removed from refrigeration, and a thin layer of the RBC–agarose solution was poured onto the gel surface to allow the entire surface to coat in a thin layer. After 5 min, the RBC–agarose layer was solidified, and the remaining agarose solution without RBCs was poured to completely fill the frame. This procedure created a thin layer of RBCs suspended in the center of the agarose phantom.

Histotripsy pulse generation

Histotripsy pulses were generated at four ultrasound frequencies (345 kHz, 500 kHz, 1.5 MHz and 3 MHz) using three custom-built histotripsy transducers. The 345-kHz pulses were generated by a 20-element array transducer with a geometric focus of 150 mm, an aperture size of 272 mm and an effective *f*-number of 0.55. The 1.5-MHz pulses were generated by a 6-element array transducer with a geometric focus of 55 mm, an aperture of 79 mm in the elevational direction and 69 mm in the lateral direction and effective *f*-numbers of 0.7 and 0.8 in the elevational and lateral directions, respectively. The 500-kHz and 3-MHz pulses were generated by a dual-frequency array transducer that consisted of twelve 500-kHz elements and seven 3-MHz elements. For the 500-kHz elements, the geometric focus was 40 mm, the aperture size was 71 mm and the effective *f*-number was 0.56. For the 3-MHz elements, the geometric focus was 40 mm, the aperture size was 80 mm and the effective *f*-number was 0.5. The design of the dual-frequency transducer was described in detail in a previous study (Lin et al. 2014a).

To compare the NMH cavitation threshold with the histotripsy intrinsic threshold, short pulses with a single dominant negative pressure half-cycle were applied to the tissue phantoms with and without nanodroplets inside a water bath heated to 37°C. To generate a short therapy pulse, a custom high-voltage pulser developed in-house was used to drive the transducers. The pulser was connected to a field-programmable gate array (FPGA) board (Altera DE0-Nano Terasic Technology, Dover, DE, USA)

specifically programmed for histotripsy therapy pulsing. This setup allowed the transducers to output short pulses of fewer than two cycles. A fiberoptic probe hydrophone built in-house (Parsons et al. 2006b) was used to measure the acoustic output pressure of the transducers. At higher pressure levels ($p- > 23$ MPa), the acoustic output could not be directly measured because of cavitation at the fiber tip. These pressures were estimated by a summation of the output focal $p-$ values from individual transducer elements. This approximation assumes that minimal nonlinear distortion of the waveform occurs within the focal region. In a previous study (Maxwell et al. 2013), this estimated $p-$ was found to be accurate within 15% compared with direct focal pressure measurements in water and in a medium (1,3-butanediol) with a higher cavitation threshold. Sample acoustic waveforms produced by the four frequency transducers are provided in Figure 2a.

Optical imaging and image processing

High-speed optical imaging was used to capture images of the focal zone after the propagation of each pulse through the focus using two high-speed cameras (Fig. 2b). For experiments with the 345-kHz and 1.5-MHz transducers, a high-speed, 1-megapixel CCD camera (Phantom V210, Vision Research, Wayne, NJ, USA) was aligned with the transducer and backlit by a continuous white-light source. The camera was focused using a macro-bellows lens (Tominon, Kyocera), giving the captured images resolutions of approximately 5.9 and 3.4 μm per pixel for 345 kHz and 1.5 MHz, respectively. For experiments with the 500-kHz and 3-MHz dual-frequency transducer, a digital, 1.3-megapixel CCD camera (PN: FL3-U3-13 Y3 M-C, Flea 3, PointGrey, Richmond, BC, Canada) was positioned perpendicularly to the dual-frequency array transducer facing one of the transducer's optical windows. A Nikon 4X objective was attached to the camera with extension tubes to magnify the image plane, giving the captured images a resolution of approximately 2.5 μm per pixel. A pulsed white-light LED was placed on the diametrically opposed optical window of the dual-frequency array transducer, which provided back-lit illumination. The cameras were triggered to record one image for each applied pulse. After acquisition, shadowgraph images were converted from gray scale to binary by an intensity threshold determined by the background intensity using image processing software (MATLAB, The MathWorks, Natick, MA, USA), as described in a previous study (Maxwell et al. 2013). Bubbles were indicated as any black regions >5 pixels. By this criterion, the minimum resolvable bubble radii were 14.75, 6.25, 8.5 and 6.25 μm for the 345-kHz, 500-kHz, 1.5-MHz and 3-MHz transducers, respectively.
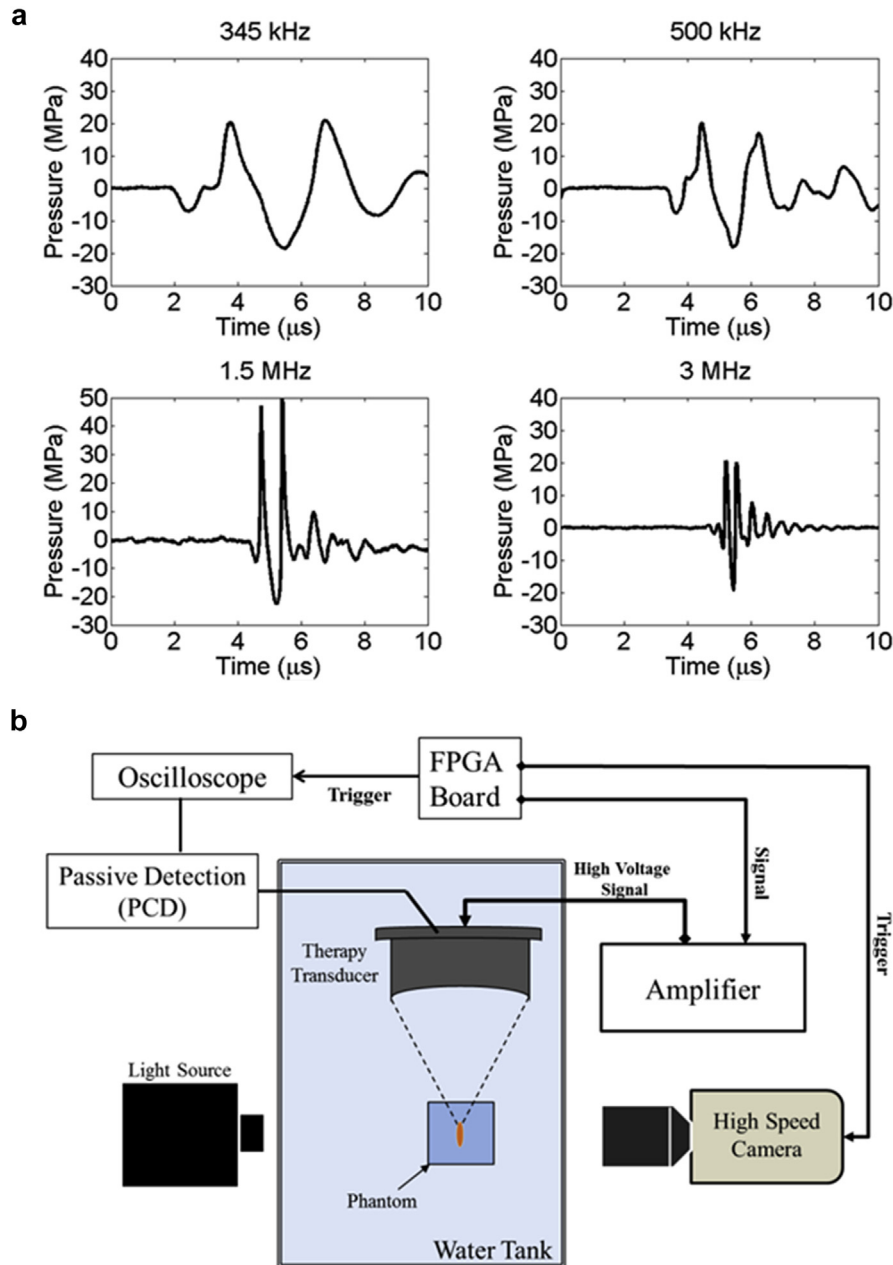
Fig. 2. (a) Example waveforms for 2-cycle histotripsy pulses generated by custom-built 345-kHz, 500-kHz, 1.5-MHz and 3-MHz transducers. (b) Experimental setup showing the focus of the histotripsy transducers aligned inside tissue phantoms containing perfluoropentane, perfluorohexane or no nanodroplets. Cavitation was monitored with high-speed optical imaging and passive cavitation detection using one of the therapy elements. FPGA = field-programmable gate array, PCD = passive cavitation detection.

Passive cavitation detection

In addition to high-speed imaging, an acoustic method was used to identify cavitation in the focal zone for cavitation threshold experiments. For each experiment, one of the transducer's therapy elements was also used for passive cavitation direction to detect the presence of cavitation in the focal region (Fig. 2b). The

passive cavitation detector (PCD) signal was connected to an oscilloscope (LT372, Lecroy, Chestnut Ridge, NY, USA) with the time window selected to record the backscattering of the therapy pulse from cavitation bubbles (Maxwell et al. 2013; Vlaisavljevich et al. 2014, 2015b). To determine whether cavitation occurred during a pulse, the signal generated by backscattering

of the incident pulse from the focus was analyzed according to the method used in previous studies (Maxwell et al. 2013; Vlaisavljevich et al. 2015b). A significant fraction of the incident wave energy is scattered when a cavitation bubble expands, greatly increasing the backscattered pressure amplitude received by the PCD. This signal appeared on the PCD at the time point corresponding to two times the time of flight for the focal length of the respective transducers. The integrated frequency power spectrum (S_{PCD}) of the backscatter signal was used as a measure of whether cavitation occurred according to the method previously described by Maxwell et al. (2013).

NMH cavitation threshold

For cavitation threshold experiments, 100 pulses were applied to each sample inside a water bath heated to 37°C at each pressure level at a PRF of 0.5 Hz. The PRF was kept low to minimize the possibility that cavitation from one pulse would change the probability of cavitation on a subsequent pulse. In a previous study, it was found that cavitation during a pulse increased the likelihood of cavitation on a subsequent pulse for PRFs >1 Hz, but this effect was not observed for PRFs <1 Hz (Maxwell et al. 2013). In addition to this low PRF, the focus was translated for each pulse by 1 mm transverse to the acoustic propagation direction in a 10×10 grid to minimize the effects of cavitation damage to the nanodroplets or tissue phantoms from alteration of the probability of cavitation. For each pulse, cavitation was monitored using both high-speed imaging and passive cavitation detection, and the fraction of total pulses (out of 100) for which cavitation was detected was determined as the cavitation probability.

The probability of observing cavitation followed a sigmoid function is given by

$$P(p_-) = \frac{1}{2} + \text{erf}\left(\frac{p_- - p_t}{\sqrt{2\sigma^2}}\right) \quad (1)$$

where erf is the error function; p_t is the negative pressure at which the probability and $p_{cav} = 0.5$; σ is a variable related to the width of the transition between $p_{cav} = 0$ and $p_{cav} = 1$, with $\pm\sigma$ giving the difference in pressure from about $p_{cav} = 0.15$ to $p_{cav} = 0.85$ for the fit (Maxwell et al. 2013). The cavitation threshold for each sample, p_t, is defined as the $p-$ corresponding to $p_{cav} = 0.5$ as calculated by the curve fit. Curve fitting for all data sets was performed using an OriginLab curve fitting program (OriginPro 9.1, OriginLab, Northampton, MA, USA). The fit curves for all samples were analyzed statistically to determine whether the differences in the values of p_t were significantly different. The standard errors for p_t were estimated by a covariance matrix using

the delta method (Hosmer and Lemeshow 1992). The curves were compared using a two-sample *t*-test with statistic $t(p_{int1} - p_{int2}, \sqrt{SE_1^2 + SE_2^2})$ at a 95% confidence interval. Results were considered statistically significant at $p < 0.05$. Note that the standard error does not include the uncertainty in absolute pressure from the hydrophone measurement, only the uncertainty in the fit. A sample size of three tissue phantoms was used for each experimental condition (*i.e.*, PFP nanodroplets, PFH nanodroplets, or no nanodroplets).

NMH multipulse sustainability

To test the hypothesis that PFH nanodroplets will remain sustainable cavitation nuclei over multiple pulses while PFP nanodroplets will be destroyed during the first few pulses, 1,000 ultrasound pulses were applied to a single focal region in tissue phantoms containing PFP and PFH nanodroplets inside a water bath heated to 37°C. Pulses were applied at a PRF of 1 Hz and peak negative pressures of 11.8 MPa (345 kHz), 12.6 MPa (500 kHz), 14.3 MPa (1.5 MHz) and 15.6 MPa (3 MHz). The PRF in this study was kept low (1 Hz) to minimize the contributions of residual nuclei from a previous pulse from effecting cavitation generation on a subsequent pulse, to determine if PFP and PFH nanodroplets continue to function as viable cavitation nuclei after the first few pulses or if the nanodroplets are destroyed in the cavitation process. Furthermore, a PRF of 1 Hz was also chosen, as previous work had shown an increase in ablation efficiency for 1-Hz treatments in comparison to higher PRF treatments that rely on residual nuclei from previous pulses to maintain the cavitation bubble cloud (Wang et al. 2012; Lin et al. 2014b). Cavitation was monitored using high-speed optical imaging, and the numbers of bubbles produced by each pulse were compared for 1,000 histotripsy pulses in each sample.

NMH RBC phantom ablation

Agarose gel phantoms with an embedded RBC layer were used to characterize cell fractionation induced by NMH. Fractionation of the RBCs turns the color of the embedded cell layer from opaque red to translucent as the RBCs are lysed, which allows direct visualization of the histotripsy-induced fractionation process (Maxwell et al. 2010). Previous studies have also indicated that the lesion visualized in RBC phantoms is similar to the lesion generated in tissue identified by histology (Maxwell et al. 2010). For RBC experiments, 2,000 histotripsy pulses were applied to the center of the red blood cell phantom layer at PRFs of 1 and 10 Hz (n = 4). The bubble cloud and resulting cell fractionation were recorded by high-speed optical imaging after each pulse.

Cell fraction was compared between RBC phantoms with PFP and PFH nanodroplets.

RESULTS

Nanodroplet characterization

In this study, we aimed to encapsulate PFH into the triblock amphiphilic $P(HDFMA_8\text{-}co\text{-}MMA_{20})\text{-}b\text{-}PAA_{12}\text{-}b\text{-}PEG_{45}$ co-polymer to compare the cavitation ability of PFH-loaded nanodroplets with that of PFP-loaded nanodroplets. In our previous study, we reported that PFP can be encapsulated in the fluorinated co-polymer, forming nanodroplets containing an elastic shell with an average size of ∼100–400 nm (Yuksel Durmaz et al. 2014). In contrast to PFP, the solubility of PFH is limited in most common polar solvents, as well as water. Moreover, PFH is not miscible with any of these solvents and exhibits clear phase separation from organic solvents. In this study, we hypothesized that PFH could be encapsulated by the $P(HDFMA_8\text{-}co\text{-}MMA_{20})\text{-}b\text{-}PAA_{12}\text{-}b\text{-}PEG_{45}$ co-polymer, forming nanodroplets with similar in size and characteristics to the PFP droplets described in our previous study (Yuksel Durmaz et al. 2014). Results indicated that both PFP and PFH encapsulated into stable nanodroplets in the desired size range (100–600 nm). NTA size analysis revealed similar characteristics for the PFP and PFH droplets (Fig. 3). PFP-loaded nanodroplets size ranged from 100–450 nm with the major peak <300 nm. The size distribution of PFH-loaded nanodroplets was slightly larger than that of PFP-loaded nanodroplets, ranging from 100 to 600 nm. Three additional high-intensity peaks in the ranges 200–300, 300–450 and 450–600 nm were observed in the large-size portion of the PFH nanodroplet size plot (Fig. 3b). The larger size of the PFH-loaded nanodroplets is possibly due to the difference in PFH miscibility with the THF/co-polymer mixture compared with PFP. For example, PFP was observed to homogenously disperse in the THF/co-polymer mixture at the beginning of droplet formulation, whereas PFH remained separate from the mixture on the bottom of the round-bottom flask. This energetically favored phase separation was broken up by dropwise addition of water to trigger the micellization process of the amphiphilic co-polymer under vigorous stirring. This strategy allowed for uniform mixing of the PFH and efficient encapsulation in the droplet core. Both types of droplets were dispersed throughout the aqueous solution without aggregation or settling down in solution due to the hydrophilic PEG corona. PFP- and PFH-loaded nanodroplets exhibited similar concentrations and size distributions (Fig. 3). The error bars on the size distribution plots represent the standard deviation of the repeat measurements of each sample. The mean sizes and standard deviations obtained by the
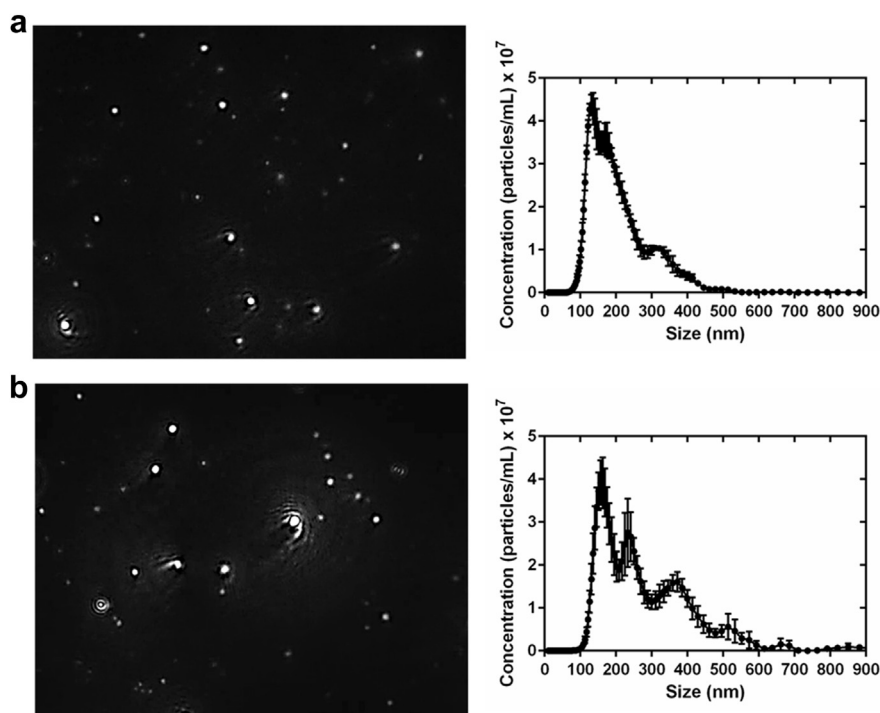

Fig. 3. Nanoparticle tracking analysis (left) revealed similar characteristics for perfluoropentane- (a) and perfluorohexane- (b) loaded nanodroplets. Size distribution plots (right) show the average size of the droplets was 177.9 ± 1.9 nm and 233.9 ± 3.9 nm for PFP and PFH nanodroplets, respectively.

NTA software correspond to arithmetical values calculated with the sizes of all particles analyzed for each sample (n = 5). Results from all samples indicated average sizes of 177.9 ± 1.9 and 233.9 ± 3.9 nm for PFP and PFH nanodroplets, respectively.

NMH cavitation threshold

To investigate the effects of nanodroplet composition on the NMH threshold, histotripsy pulses were applied to tissue-mimicking agarose phantoms with PFP nanodroplets, PFH nanodroplets, and no nanodroplets using the 345-kHz, 500-kHz, 1.5-MHz, and 3-MHz histotripsy transducers. For all experimental conditions, cavitation bubbles were observed on the high-speed camera in an increasingly larger area with increasing pressure once a certain negative pressure was exceeded, with complete agreement between optical imaging and passive cavitation detection methods (Fig. 4), as seen in previous studies (Maxwell et al. 2013; Vlaisavljevich et al. 2015b). Plotting the probability of cavitation as a function of peak negative pressure revealed a significant decrease in the cavitation threshold with both PFP and PFH nanodroplets compared with controls at all frequencies (Fig. 5). Additionally, results revealed a slight increase in the nanodroplet cavitation threshold for PFH nanodroplets compared with PFP nanodroplets (Fig. 5). Cavitation threshold results for all experimental conditions are listed in Table 1. Comparing the threshold results for phantoms containing PFH nanodroplets with those for control phantoms indicated that the cavitation threshold was decreased by 14.4, 15, 13.7 and 11.9 MPa at 345 kHz, 500 kHz, 1.5 MHz and 3 MHz, respectively (Fig. 6). When phantoms containing PFP and PFH

nanodroplets were compared (Fig. 6), decreases of 3, 1.3, 2.5 and 1.7 MPa were observed for PFP phantoms at 345 kHz, 500 kHz, 1.5 MHz and 3 MHz, respectively (Fig. 6). For all experimental conditions, the cavitation threshold decreased at lower frequency, as has been observed in previous studies (Fig. 6) (Vlaisavljevich et al. 2013a, 2015b). A two-way analysis of variance performed on the data illustrated in Figure 6 revealed that all differences between the cavitation thresholds in PFP, PFH, and control phantoms were significant ($p < 0.05$).

NMH multipulse sustainability

To compare the ability of nanodroplets to act as sustainable cavitation nuclei over multiple pulses, 1,000 histotripsy pulses were applied to a single focal region in phantoms containing PFP and PFH nanodroplets at a PRF of 1 Hz. Results indicated that a bubble cloud consisting of many bubbles was observed after the first pulse for both types of droplets (Fig. 7). However, the bubble cloud generated in PFH phantoms was a more well-defined bubble cloud, similar to those previously observed for histotripsy above the intrinsic threshold (Vlaisavljevich et al. 2015b, 2015c). At all frequencies, over all 1,000 pulses, a dense bubble cloud was produced in PFH phantoms, with the bubbles more tightly confined inside the focal region and no significant change in the number of bubbles inside the cloud (Figs. 7 and 8). In comparison, after the first pulse, the bubble cloud generated in the PFP phantom was sparsely populated (Figs. 7 and 8). At all frequencies, the number of bubbles observed inside PFP phantoms significantly decreased with increasing number of pulses,
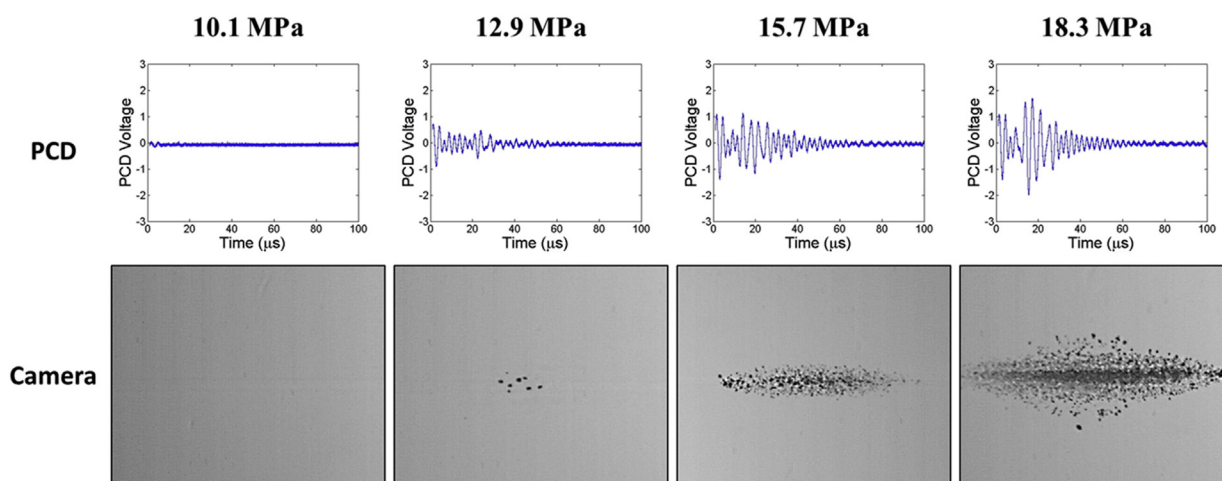

Fig. 4. Cavitation detection. Sample passive cavitation detection (PCD) signals (top) and high-speed optical imaging (bottom) were used for cavitation detection for cavitation threshold experiments. Results indicated good agreement between the two methods. Representative images shown above are from application of 1.5-MHz histotripsy pulses to tissue phantoms containing perfluorohexane nanodroplets.
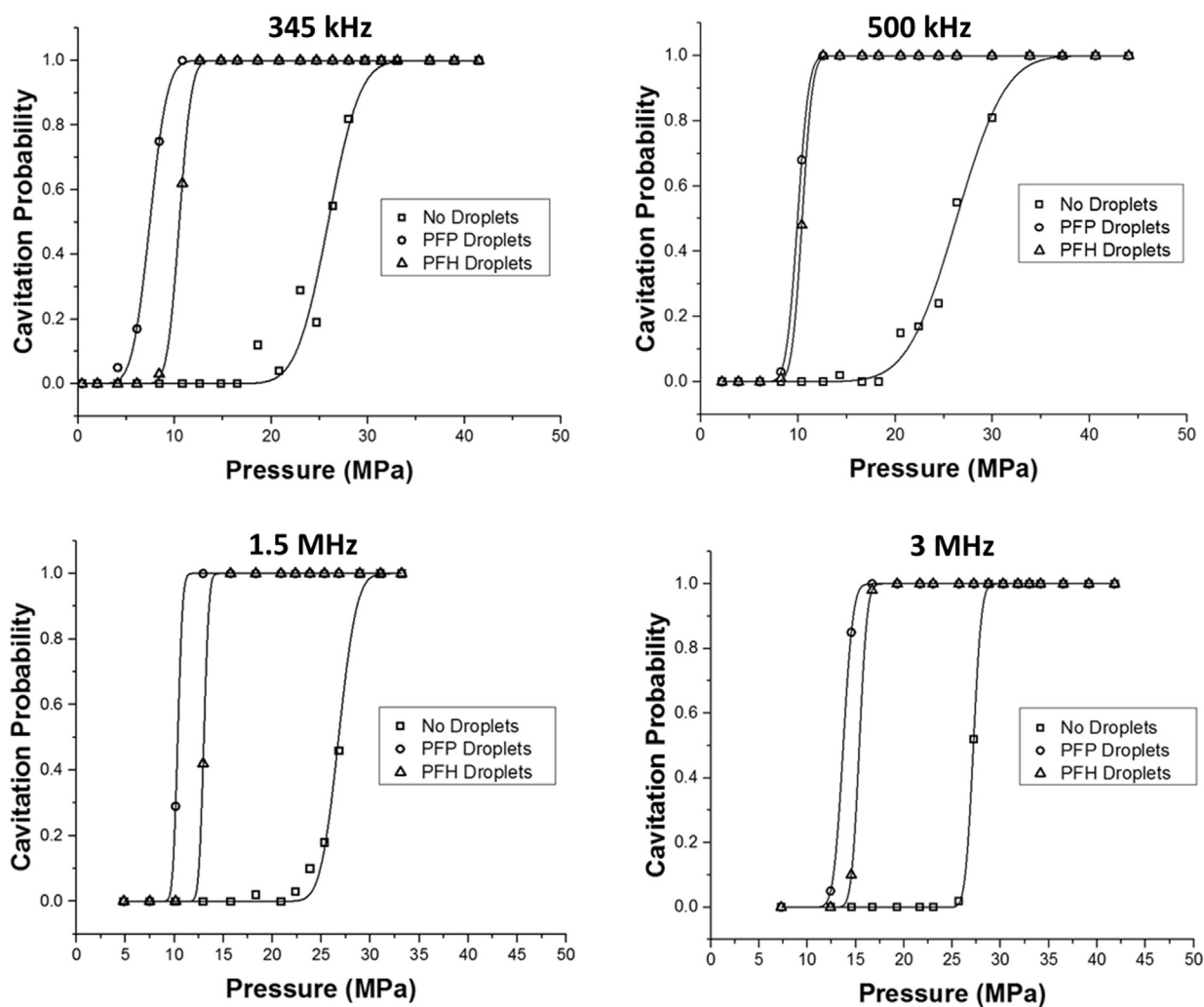
Fig. 5. Sample cavitation probability curves for tissue phantoms containing perfluoropentane (PFP) nanodroplets, perfluorohexane (PFH) nanodroplets and no nanodroplets at 345 kHz, 500 kHz, 1.5 MHz and 3 MHz. At all frequencies, results indicated a significant decrease in the cavitation threshold with both PFP and PFH nanodroplets compared with controls. Results also indicated a slight increase in the nanodroplet cavitation threshold for PFH nanodroplets compared with PFP nanodroplets.

and bubbles were extinguished after ∼5–50 pulses. At a higher frequency, the bubbles were extinguished after fewer pulses. For example, no bubbles were observed after ∼50 pulses in PFP phantoms exposed to 500 kHz ($p-$ = 12.6 MPa) pulses and after ∼5 pulses in the PFP phantoms exposed to 3 MHz ($p-$ = 15.6 MPa) pulses.

NMH RBC phantom ablation

Agarose tissue phantoms embedded with RBC layers were used to compare NMH ablation for phantoms containing PFP and PFH nanodroplets. Results indicated that NMH generated consistent, well-defined lesions for RBC phantoms containing PFH nanodroplets, with the results being consistent for NMH treatments applied at

1- and 10-Hz PRFs. For example, Figures 9 and 10 are images of NMH lesions generated inside RBC phantoms containing PFH droplets using the 345-kHz (Fig. 9) and 1.5-MHz (Fig. 10) transducers. For all cases, dense cavitation bubble clouds were generated inside the PFH phantom on every pulse, resulting in sharp lesions with well-defined boundaries between the fractionated lesion and intact RBCs (Figs. 9 and 10). In contrast, only sparse lesions were formed inside the PFP phantoms. For example, for the 10-Hz-PRF treatments using the 345-kHz transducer, sparse cavitation bubble clouds were observed over the course of the treatment, with the location of the bubbles remaining consistent from pulse to pulse inside the PFP phantoms, resulting in sparse lesions (Fig. 9). For the 1-Hz treatments inside the PFP phantoms

Table 1. Threshold results: Peak negative pressure, p_t, at which the fit curve set $p_{cav} = 0.5$ for each sample, as well as the mean values for p_t and σ*

Frequency	Material	p_t (1)	p_t (2)	p_t (3)	p_t (mean)	σ (mean)
345 kHz	No droplets	25.9	23.7	24.7	24.8	2.0
	PFP droplets	7.3	7.4	7.4	7.4	1.4
	PFH droplets	10.5	10.1	10.6	10.4	0.9
500 kHz	No droplets	23.5	26.3	26.7	25.5	1.8
	PFP droplets	9.4	10.0	8.2	9.2	0.8
	PFH droplets	10.4	10.8	10.3	10.5	0.8
1.5 kHz	No droplets	26.8	27.0	26.3	26.7	1.0
	PFP droplets	10.3	10.7	10.5	10.5	0.4
	PFH droplets	12.8	13.0	13.1	13.0	0.3
3 MHz	No droplets	26.9	27.2	26.3	26.8	0.9
	PFP droplets	13.1	12.9	13.7	13.2	0.6
	PFH droplets	14.6	14.6	15.4	14.9	0.4

PFH = perfluorohexane; PFP = perfluoropentane.

* A two-way analysis of variance indicated that all differences in p_{t_mean} between samples were statistically significant ($p < 0.05$).

using the 345-kHz transducer, cavitation was observed only on the initial pulses (<10 pulses) and was not maintained for the duration of the treatment, resulting in very small lesions after treatment (Fig. 9). At higher frequency (*i.e.*, 1.5 MHz), no visible lesions were observed in the PFP phantoms for either 1- or 10-Hz treatments, with bubbles only visible on the first pulse (Fig. 10). Quantifying the lesion areas for RBC phantoms (n = 4) revealed a significant decrease in lesion size for phantoms containing PFP droplets as compared with PFH phantoms. For example, at 345 kHz, the lesion areas inside the PFH phantoms were 14.35 ± 1.13 mm^2 (1 Hz) and 15.01 ± 1.61 mm^2 (10 Hz), which were significantly larger than the lesion areas inside the PFP phantoms of 0.05 ± 0.04 mm^2 (1 Hz) and 3.24 ± 0.29 mm^2 (10 Hz). At 1.5 MHz, the lesion areas inside the PFH phantoms were 1.31 ± 0.09 mm^2 (1 Hz) and 1.17 ± 0.13 mm^2 (10 Hz), which were significantly larger than the lesion areas inside the PFP phantoms of 0.00 ± 0.00 mm^2 (1 Hz, 10 Hz).
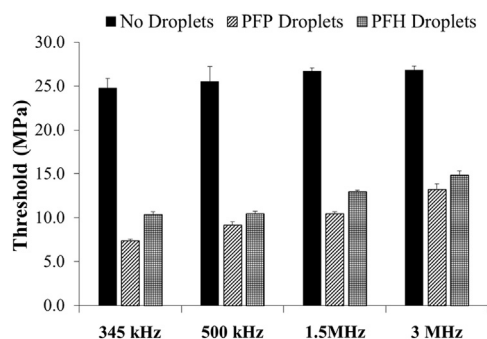

Fig. 6. Bar plots illustrate the complete cavitation threshold results for tissue phantoms containing perfluoropentane (PFP) nanodroplets, perfluorohexane (PFH) nanodroplets and no nanodroplets. All differences in the cavitation threshold between samples were statistically significant ($p < 0.05$).

DISCUSSION

In this study, the effects of droplet composition on NMH therapy were investigated using perfluoropentane (boiling point ~29°C, surface tension ~9.5 mN/m) and perfluorohexane (boiling point ~56°, surface tension ~11.9 mN/m) nanodroplets. In the first part of this study, PFP and PFH droplets were synthesized using a previous developed method (Yuksel Durmaz et al. 2014). The results from the nanodroplet characterization suggest that the droplet preparation method described by Yuksel Durmaz et al. (2014) can be used to create nanodroplets with similar surface characteristics within the media while the composition of the encapsulated perfluoro-carbon can be modulated as desired. The design of the tri-block amphiphilic copolymer acts to increase the particle's solubility in aqueous environments because of the hydrophilic character of the outer PEG block, while also improving hemocompatibility (*i.e.*, no protein adsorption on the particles, no macrophage recognition and minimum interaction with blood cells during blood circulation) (Dobrovolskaia et al. 2008; Kim et al. 2005; Yuksel Durmaz et al. 2014). The results of this study suggest that the PFC inside the nanodroplets can be easily modified to take advantage of perfluorocarbons with different boiling points without losing the benefits of the functionalized polymer shell.

In the second part of this study, the effects of droplet composition on the histotripsy cavitation threshold were investigated, with results indicating a significant decrease in the cavitation threshold for both types of nanodroplets compared with controls, with a slightly lower threshold observed for PFP phantoms, likely because of the decrease in surface tension for PFP. These results support our hypothesis that both PFP and PFH nanodroplets can be used to significantly reduce the pressure required to generate histotripsy bubbles for NMH therapy. At all frequencies tested, the NMH threshold for both types of droplets was significantly lower (>10-MPa decrease) than the histotripsy intrinsic threshold, while maintaining steep threshold behavior. In fact, the σ_{mean} values calculated by the curve fit decreased (*i.e.*, sharper threshold curve) for phantoms containing nanodroplets, with the lowest σ_{mean} values observed for phantoms containing PFH droplets (Table 1). This distinct threshold behavior is promising for the development of NMH therapy in which the applied pressure must be chosen in the region above the NMH threshold, but below the histotripsy intrinsic threshold, to ensure cavitation is generated only in regions containing nanodroplets. The results of these threshold experiments suggest that both PFP and PFH nanodroplets could be used for NMH, with PFP droplets offering a slightly lower threshold (~1- to 3-MPa decrease). With everything else equal, one might
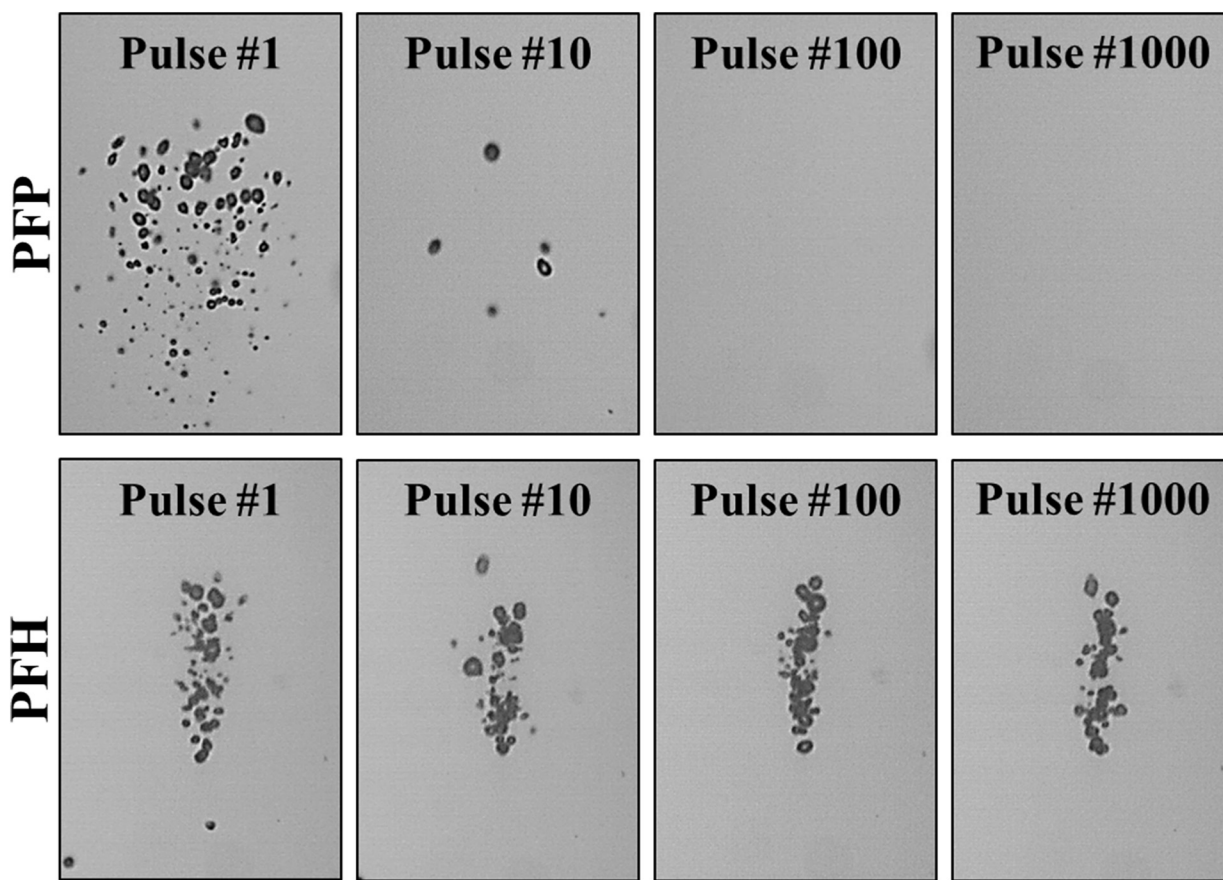
Fig. 7. Optical images of nanodroplet-mediated histotripsy bubbles produced by 500-kHz ($p-$ = 12.6 MPa) pulses at a single focal point in tissue phantoms containing perfluoropentane (PFP) and perfluorohexane (PFH) nanodroplets at a pulse repetition frequency of 1 Hz. Results for PFP phantoms revealed a decrease in the number of bubbles observed at the focus with increasing pulse number, with no bubble observed after ~50 pulses. PFH phantom results revealed no significant decrease in the number of bubbles observed at the focus with increasing pulse number, with well-defined dense bubble clouds still observed after 1,000 pulses.

expect a lower cavitation threshold for the larger PFH droplets (233.9 ± 3.9 nm) compared with PFP droplets (177.9 ± 1.9 nm). It is possible that the slight decrease in threshold for PFP droplets is due to the lower surface tension of PFP (9.5 mN/m) compared with PFH (11.9 mN/m), as previous work has indicated that the cavitation threshold is highly dependent on the surface tension of the media (*i.e.*, bulk fluid inside the droplet) when using the 1-2 cycle pulses used in this study (Maxwell et al. 2013; Vlaisavljevich et al. 2015b). These results suggest that the nanodroplets may actually decrease the cavitation threshold by carrying a lower threshold medium, rather than each droplet acting as single cavitation nucleus as would be the case for an air contrast agent. On the basis of this finding, the results of this work suggest that the NMH threshold can be selectively modulated by changing the droplet composition, with lower surface-tension/boiling-point droplets resulting in a decreased cavitation threshold.

The finding that the NMH threshold can be finely tuned by changing droplet composition while maintaining the distinct threshold behavior is a significant benefit for the development of NMH therapy, as well as for other nanodroplet applications such as selective drug delivery (Fabiilli et al. 2013).

In the final part of this study, the effects of droplet composition on cavitation sustainability and tissue fractionation were investigated, with results indicating that PFH nanodroplets were sustainable cavitation nuclei over multiple pulses, whereas PFP nanodroplets were destroyed during the initial pulses. This effect resulted in well-defined lesions being generated inside the red blood cell phantom containing PFH droplets under all treatment conditions. In contrast, only sparse lesions were formed inside the PFP phantoms for the 345-kHz treatments applied at 10-Hz PRF, with no visible lesions observed at higher frequency (*i.e.*, 1.5 MHz) or lower PRF (*i.e.*, 1 Hz). The increased cavitation sustainability of the
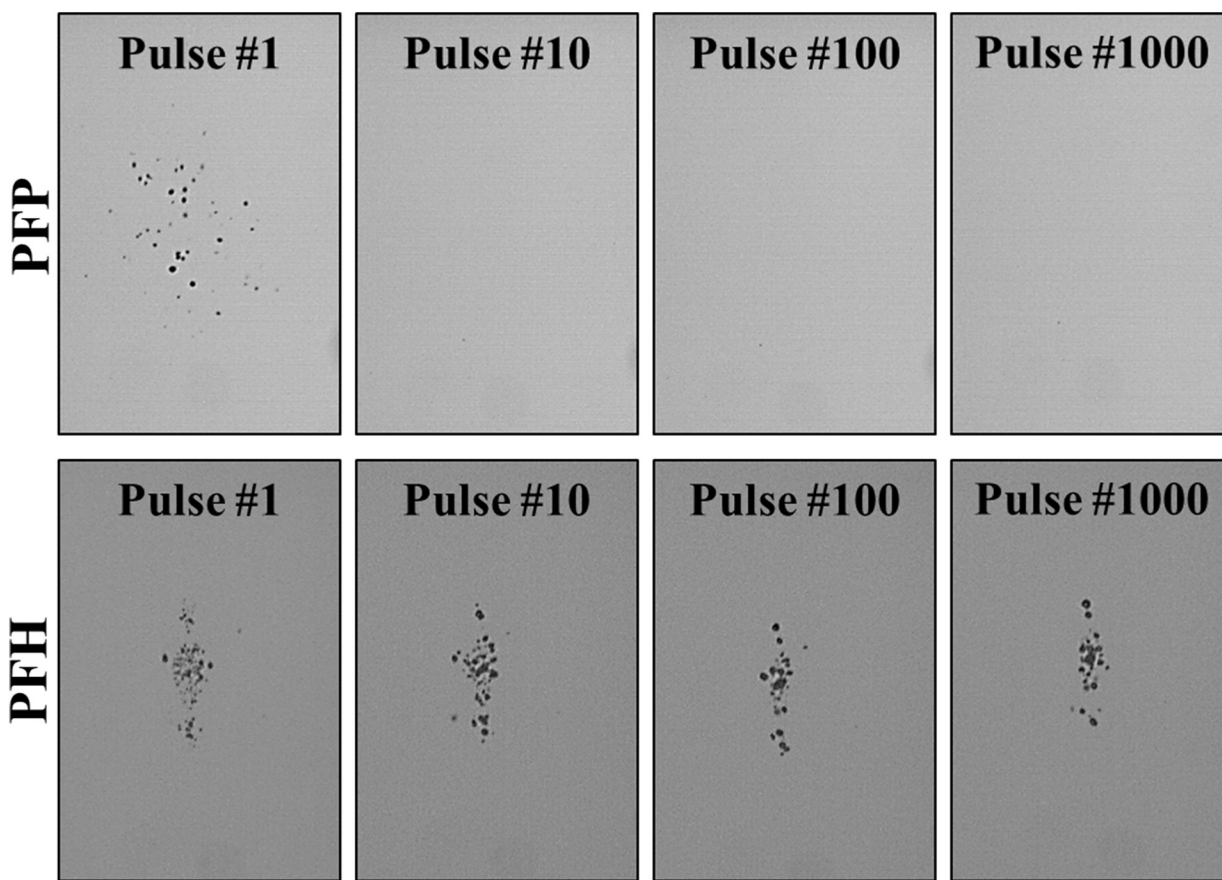
Fig. 8. Optical images of nanodroplet-mediated histotripsy (NMH) bubbles produced by 3-MHz ($p- = 15.6$ MPa) pulses at a single focal point in tissue phantoms containing perfluoropentane (PFP) and perfluorohexane (PFH) nanodroplets at a pulse repetition frequency of 1 Hz. Results for PFP phantoms revealed a decrease in the number of bubbles observed at the focus with increasing pulse number, with no bubble observed after ~5 pulses. PFH phantom results revealed well-defined NMH bubble clouds were still observed after 1,000 pulses.

PFH droplets is most likely due to the re-condensing of PFH droplets into a liquid after the cavitation event occurs, because of the higher boiling point of the PFH droplets. The finding that PFH nanodroplets act as sustainable cavitation nuclei over multiple pulses, whereas PFP droplets are destroyed during the initial pulses, supports our hypothesis that using droplets with a higher boiling point is advantageous for NMH therapy. Results suggest that PFH droplets may re-condense into a liquid after collapse of the cavitation bubble, whereas the PFP bubbles are destroyed by the cavitation process (*i.e.*, do not return to liquid form). These results suggest that higher-boiling-point droplets can be used to significantly reduce the nucleation threshold for generating cavitation bubbles over multiple pulses, allowing NMH therapy to be applied for multiple pulses until the targeted tissue is completely fractionated, even at low PRF. In contrast, because of the lower boiling point, PFP nanodroplets are only capable of reducing the cavitation threshold on the initial pulses, requiring cavitation on subsequent pulses to be generated from residual nuclei remaining in the focal region from previous pulses. The finding that higher-boiling-point droplets can serve as functional cavitation nuclei over multiple pulses is therefore a major benefit for NMH therapy, as previous work has indicated a decrease in ablation efficiency for higher-PRF treatments that rely on residual nuclei from previous pulses to maintain the cavitation bubble cloud (Wang et al. 2012).

In addition to the finding that PFH droplets acted as sustainable cavitation nuclei over multiple pulses, it was also observed that the NMH bubble clouds produced from PFH droplets were better defined and more densely populated compared with the sparse bubble clouds produced by the PFP droplets, even when comparing bubble clouds produced on the first pulse. The well-confined, dense bubble clouds produced inside the PFH phantoms closely match the behavior of bubble clouds previously observed for histotripsy treatments above the intrinsic threshold, which have been shown to be efficient and precise at fractionating the target tissue (Lin et al. 2014b; Maxwell et al.
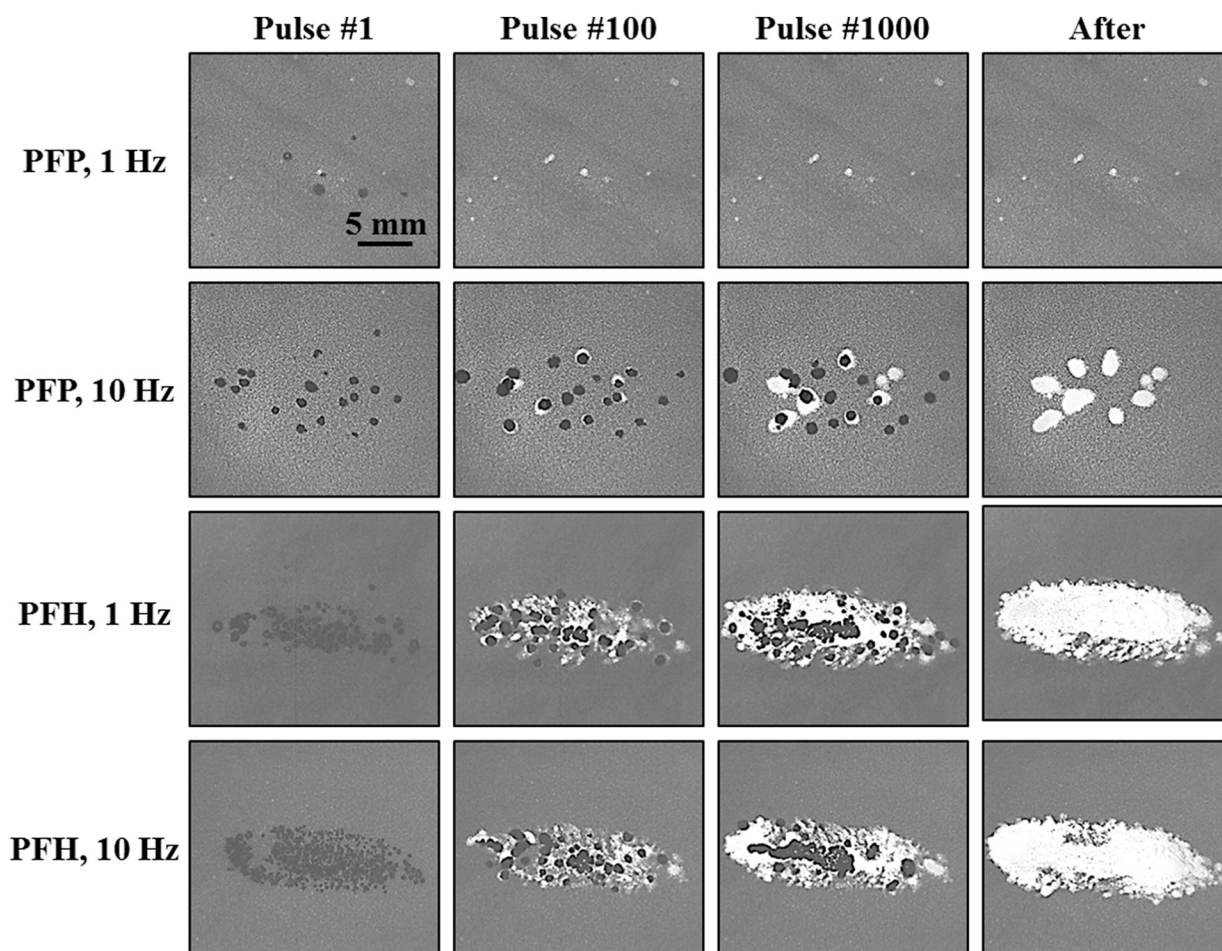
Fig. 9. Optical images of nanodroplet-mediated histotripsy fractionation produced by 345-kHz ($p-$ = 12.6 MPa) pulses in red blood cell phantoms containing perfluoropentane (PFP) and perfluorohexane (PFH) nanodroplets at pulse repetition frequencies of 1 and 10 Hz. Results revealed significantly larger and more well-defined lesions generated inside the PFH tissue phantoms, compared with the sparse lesions inside the PFP tissue phantoms.

2013; Vlaisavljevich et al. 2015b, 2015c). In contrast, the more sparse bubble clouds produced inside the PFP phantoms resemble bubble clouds generated at higher PRF or bubble clouds that rely on residual nuclei to maintain cavitation, which have been found to be less efficient at fractionating tissue while increasing collateral damage to surrounding tissue (Wang et al. 2012). This observation suggested that NMH bubble clouds produced using PFH droplets will be more efficient at fractionating tissue and provide less collateral damage to surrounding tissue compared with NMH therapy using PFP droplets, which was validated by the final set of experiments in this study comparing NMH ablation in red blood cell phantoms.

CONCLUSIONS

In this work, the effects of droplet composition on NMH therapy were investigated using perfluoropentane (boiling point ~29°C, surface tension ~9.5 mN/m) and perfluorohexane (boiling point ~56°, surface tension ~11.9 mN/m) droplets. The results indicated a significant decrease in the cavitation threshold for both types of nanodroplets compared with controls, with a slightly lower threshold observed for PFP phantoms, likely because of the decrease in surface tension for PFP. Results further indicated that PFH nanodroplets were sustainable cavitation nuclei over multiple pulses, whereas PFP nanodroplets were destroyed during the initial pulses. This effect is most likely due to the recondensing of PFH droplets into a liquid after the cavitation event occurs, because of the higher boiling point of the PFH droplets. In the final part of this study, tissue phantoms containing a layer of embedded red blood cells were used to compare the damage generated for NMH treatments using PFP and PFH droplets, with results indicating that PFH nanodroplets significantly improved NMH ablation, allowing
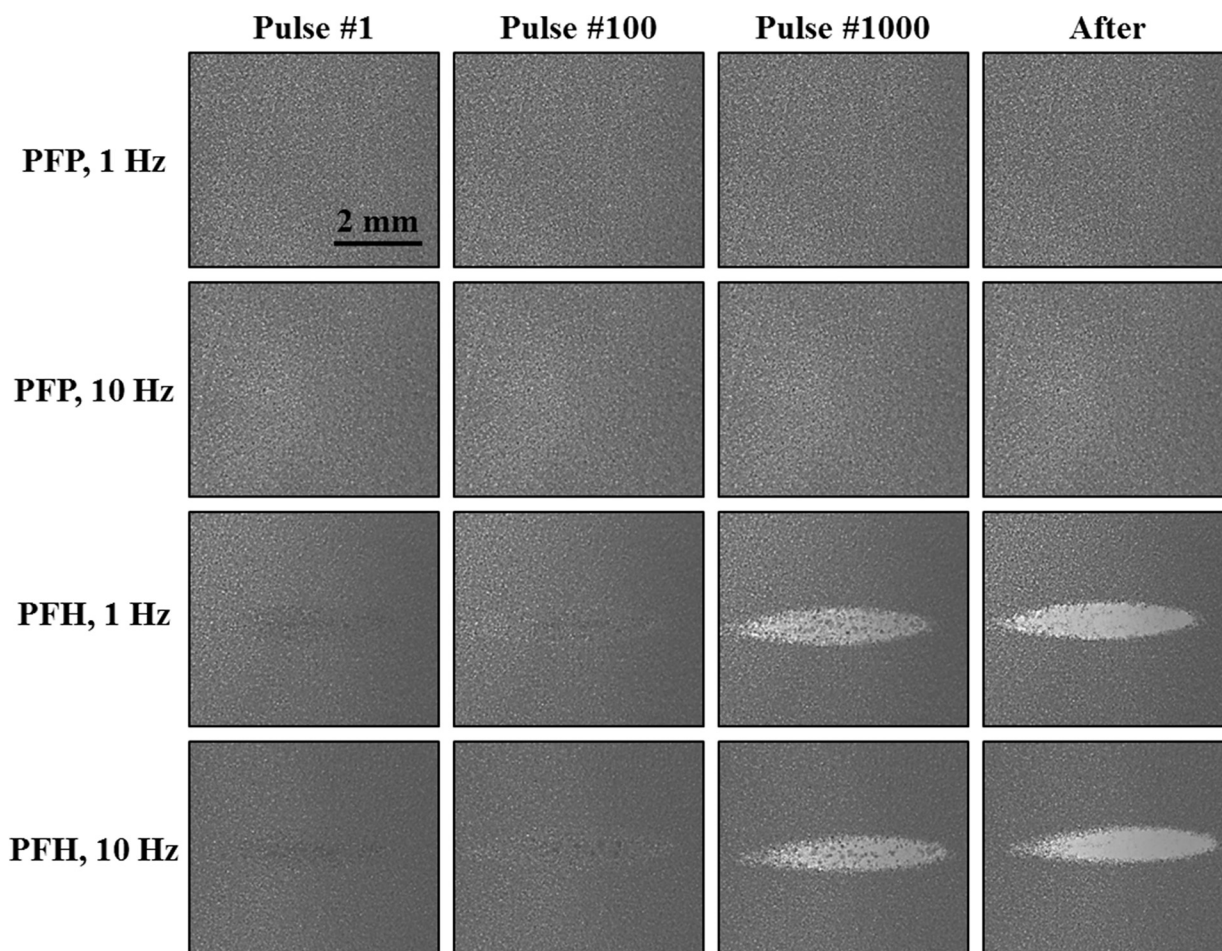
Fig. 10. Optical images of nanodroplet-mediated histotripsy fractionation produced by 1.5-MHz ($p-$ = 15.7 MPa) pulses in red blood cell phantoms containing perfluoropentane (PFP) and perfluorohexane (PFH) nanodroplets at pulse repetition frequencies of 1 and 10 Hz. Results revealed well-defined lesions generated inside the PFH tissue phantoms. No visible lesions were observed for treatments applied to tissue phantoms containing PFP droplets.

well-defined lesions to be generated at all frequencies and PRFs tested. The results of this study suggest that NMH therapy can be significantly enhanced by modulating droplet composition to optimize the cavitation threshold (decrease droplet surface tension) and increase the multipulse sustainability (increase droplet boiling point). Overall, the results of this study provide significant insight into the role of droplet composition in NMH therapy and will provide a rational basis to specifically tailor droplet parameters to improve NMH tissue fractionation.

REFERENCES

Dobrovolskaia MA, Aggarwal P, Hall JB, McNeil SE. Preclinical studies to understand nanoparticle interaction with the immune system and its potential effects on nanoparticle biodistribution. Mol Pharm 2008;5:487–495.

Fabiilli ML, Haworth KJ, Fakhri NH, Kripfgans OD, Carson PL, Fowlkes JB. The role of inertial cavitation in acoustic droplet vaporization. IEEE Trans Ultrason Ferroelectr Freq Control 2009;56: 1006–1017.

Fabiilli ML, Wilson CG, Padilla F, Martin-Saavedra FM, Fowlkes JB, Franceschi RT. Acoustic droplet–hydrogel composites for spatial and temporal control of growth factor delivery and scaffold stiffness. Acta Biomater 2013;9:7399–7409.

Giesecke T, Hynynen K. Ultrasound-mediated cavitation thresholds of liquid perfluorocarbon droplets *in vitro*. Ultrasound Med Biol 2003;29:1359–1365.

Hall TL, Kieran K, Ives K, Fowlkes JB, Cain CA, Roberts WW. Histotripsy of rabbit renal tissue *in vivo*: temporal histologic trends. J Endourol 2007;21:1159–1166.

Hempel CR, Hall TL, Cain CA, Fowlkes JB, Xu Z, Roberts WW. Histotripsy fractionation of prostate tissue: Local effects and systemic response in a canine model. J Urol 2011;185:1484–1489.

Hosmer DW, Lemeshow S. Confidence interval estimation of interaction. Epidemiology 1992;3:452–456.

Kim D, El-Shall H, Dennis D, Morey T. Interaction of PLGA nanoparticles with human blood constituents. Colloids Surf B Biointerfaces 2005;40:83–91.

Lin KW, Duryea AP, Kim Y, Hall TL, Xu Z, Cain CA. Dual-beam histotripsy: A low-frequency pump enabling a high-frequency probe for precise lesion formation. IEEE Trans Ultrason Ferroelectr Freq Control 2014a;61:325–340.

Lin KW, Kim Y, Maxwell AD, Wang TY, Hall TL, Xu Z, Fowlkes JB, Cain CA. Histotripsy beyond the intrinsic cavitation threshold using very short ultrasound pulses: Microtripsy. IEEE Trans Ultrason Ferroelectr Freq Control 2014b;61:251–265.

Maxwell AD, Wang TY, Yuan LQ, Duryea AP, Xu Z, Cain CA. A tissue phantom for visualization and measurement of ultrasound-induced cavitation damage. Ultrasound Med Biol 2010;36:2132–2143.

Maxwell AD, Owens G, Gurm HS, Ives K, Myers DD Jr, Xu Z. Noninvasive treatment of deep venous thrombosis using pulsed ultrasound cavitation therapy (histotripsy) in a porcine model. J Vasc Interv Radiol 2011;22:369–377.

Maxwell AD, Cain CA, Hall TL, Fowlkes JB, Xu Z. Probability of cavitation for single ultrasound pulses applied to tissues and tissue-mimicking materials. Ultrasound Med Biol 2013;39:449–465.

Owens GE, Miller RM, Ensing G, Ives K, Gordon D, Ludomirsky A, Xu Z. Therapeutic ultrasound to noninvasively create intracardiac communications in an intact animal model. Catheter Cardiovasc Interv 2011;77:580–588.

Parsons JE, Cain CA, Abrams GD, Fowlkes JB. Pulsed cavitational ultrasound therapy for controlled tissue homogenization. Ultrasound Med Biol 2006a;32:115–129.

Parsons JE, Cain CA, Fowlkes JB. Cost-effective assembly of a basic fiber-optic hydrophone for measurement of high-amplitude therapeutic ultrasound fields. J Acoust Soc Am 2006b;119:1432–1440.

Parsons JE, Cain CA, Fowlkes JB. Spatial variability in acoustic backscatter as an indicator of tissue homogenate production in pulsed cavitational ultrasound therapy. IEEE Trans Ultrason Ferroelectr Freq Control 2007;54:576–590.

Rapoport NY, Kennedy AM, Shea JE, Scaife CL, Nam KH. Controlled and targeted tumor chemotherapy by ultrasound-activated nanoemulsions/microbubbles. J Controlled Release 2009;138:268–276.

Roberts WW, Hall TL, Ives K, Wolf JS Jr, Fowlkes JB, Cain CA. Pulsed cavitational ultrasound: A noninvasive technology for controlled tissue ablation (histotripsy) in the rabbit kidney. J Urol 2006;175:734–738.

Sheeran PS, Luois S, Dayton PA, Matsunaga TO. Formulation and acoustic studies of a new phase-shift agent for diagnostic and therapeutic ultrasound. Langmuir 2011;27:10412–10420.

Styn NR, Wheat JC, Hall TL, Roberts WW. Histotripsy of VX-2 tumor implanted in a renal rabbit model. J Endourol 2010;24:1145–1150.

Vlaisavljevich E, Durmaz YY, Maxwell A, Elsayed M, Xu Z. Nanodroplet-mediated histotripsy for image-guided targeted ultrasound cell ablation. Theranostics 2013a;3:851–864.

Vlaisavljevich E, Kim Y, Allen S, Owens G, Pelletier S, Cain C, Ives K, Xu Z. Image-guided non-invasive ultrasound liver ablation using histotripsy: Feasibility study in an *in vivo* porcine model. Ultrasound Med Biol 2013b;39:1398–1409.

Vlaisavljevich E, Maxwell A, Warnez M, Johnsen E, Cain CA, Xu Z. Histotripsy-induced cavitation cloud initiation thresholds in tissues of different mechanical properties. IEEE Trans Ultrason Ferroelectr Freq Control 2014;61:341–352.

Vlaisavljevich E, Aydin O, Durmaz YY, Lin KW, Fowlkes JB, Elsayed M, Xu Z. The effects of ultrasound frequency on nanodroplet-mediated histotripsy. Ultrasound Med Biol 2015a;41:2135–2147.

Vlaisavljevich E, Lin KW, Maxwell A, Warnez M, Mancia L, Singh R, Putnam A, Fowlkes JB, Johnsen E, Cain C, Xu Z. Effects of ultrasound frequency and tissue stiffness on the histotripsy intrinsic threshold for cavitation. Ultrasound Med Biol 2015b;41:1651–1667.

Vlaisavljevich E, Lin KW, Warnez M, Singh R, Mancia L, Putnam A, Johnsen E, Cain C, Xu Z. Effects of tissue stiffness, ultrasound frequency, and pressure on histotripsy-induced cavitation bubble behavior. Phys Med Biol 2015c;60:2271–2292.

Wang TY, Xu Z, Hall TL, Fowlkes JB, Cain CA. An efficient treatment strategy for histotripsy by removing cavitation memory. Ultrasound Med Biol 2012;38:753–766.

Xu Z, Fowlkes JB, Ludomirsky A, Cain CA. Investigation of intensity thresholds for ultrasound tissue erosion. Ultrasound Med Biol 2005a;31:1673–1682.

Xu Z, Fowlkes JB, Rothman ED, Levin AM, Cain CA. Controlled ultrasound tissue erosion: The role of dynamic interaction between insonation and microbubble activity. J Acoust Soc Am 2005b;117:424–435.

Xu Z, Owens G, Gordon D, Cain C, Ludomirsky A. Noninvasive creation of an atrial septal defect by histotripsy in a canine model. Circulation 2010;121:742–749.

Yuksel Durmaz Y, Vlaisavljevich E, Xu Z, ElSayed M. Development of nanodroplets for histotripsy-mediated cell ablation. Mol Pharm 2014;11:3684–3695.